

Sediment Micromechanics in Sheet Flows Induced by Asymmetric Waves: A CFD–DEM Study

Rui Sun, Heng Xiao*

Department of Aerospace and Ocean Engineering, Virginia Tech, Blacksburg, VA 24060, United States

Abstract

Understanding the sediment transport in oscillatory flows is essential to the investigation of the overall sediment budget for coastal regions. This overall budget is crucial for the prediction of the morphological change of the coastline in engineering applications. Since the sediment transport in oscillatory flows is dense particle-laden flow, appropriate modeling of the particle interaction is critical. Although traditional two-fluid approaches have been applied to the study of sediment transport in oscillatory flows, the approaches do not resolve the interaction of the particles. Particle-resolved modeling of sediment transport in oscillatory flows and the study of micromechanics of sediment particles (e.g., packing and contact force) are still lacking. In this work, a parallel CFD–DEM solver *SediFoam* that can resolve the inter-particle collision is applied to study the granular micromechanics of sediment particles in oscillatory flows. The results obtained from the CFD–DEM solver are validated by using the experimental data of coarse and medium sands. The comparison with experimental results suggest that the flow velocity, the sediment flux and the net sediment transport rate predicted by *SediFoam* are satisfactory. Moreover, the micromechanic quantities of the sediment bed are presented in detail, including the Voronoi concentration, the coordination number, and the particle interaction force. It is demonstrated that variation of these micromechanic quantities at different phases in the oscillatory cycle is significant, which is due to different responses of the sediment bed. To investigate the structural properties of the sediment bed, the correlation of the Voronoi volume fraction and coordination number are compared to the results from the fluidized

*Corresponding author. Tel: +1 540 231 0926

Email addresses: sunrui@vt.edu (Rui Sun), hengxiao@vt.edu (Heng Xiao)

bed simulations. The consistency in the comparison indicates the structural micromechanics of sediment transport and fluidized bed are similar despite the differences in flow patterns. From the prediction of the CFD–DEM model, we observed that the coordination number in rapid sheet flow layer is larger than one, which indicates that a typical particle in the sediment layer is in contact with more than one particles, and thus the binary collision model commonly used in two-fluid approaches may underestimate the contact between the particles.

Keywords: CFD–DEM, sediment transport, particle-laden flow, granular micromechanics, oscillatory sheet-flow

1. Introduction

Oscillatory sheet-flow sediment transport is important in coastal and geotechnical engineering because it carries significant amount of sand and has a considerable impact on the overall sediment budget (Malarkey et al., 2009). Since the inter-particle collision plays an important role in oscillatory sheet-flow sediment transport, understanding the mechanics at the particle scale can provide physical insights of this problem. The microscopic information can describe the properties of the sediment bed, such as packing, mixing, and permeability (Yi et al., 2011). In addition, the structural strength of the seabed, without which the sediment particles will behave as fluid (Scholtès et al., 2015), can be also evaluated by using micromechanic variables. There is also an increasing interest to seek for the constitutive laws for dense granular flows in the macroscopic modeling of sediment transport problems based on the microscopic information, including the understanding of the anisotropic nature of the soil, the response of the sediment bed under stress, and the relationship between particle-scale response and material response (O’Sullivan, 2011).

1.1. *Sediment Transport in Oscillatory Sheet-Flow*

The wave orbital motion is dominant in cross-shore sediment transport (Ribberink, 1998). The wave-induced oscillatory flow may lead to onshore or offshore sediment transport, and thus is important in the prediction of beach-profile changes. Although some researchers performed experimental studies of the sediment transport in oscillatory flows, the measurement of the concentration and velocity of sediment particles are still considered very difficult (Flores and Sleath, 1998; O’Donoghue

and Wright, 2004a,b). For example, O’Donoghue and Wright (2004b) used both conductivity concentration measurement (CCM) probes and suction samplers to measure the sediment concentration. Conductivity concentration probes are used to measure the sediment concentration in the region of high concentration in the sheet flow layer, whereas suction samplers are used in the low concentration region in the suspension layer. The samplers are located at approximately one centimeter above the sediment bed to avoid the possible interaction of suction sampler and sediment bed. Therefore, the regions with medium concentration cannot be measured and there is a gap above the sediment bed in the experimental measurement data. Because of the difficulties in the experimental measurements, numerical simulations have been a cost-effective approach to study the sediment transport in oscillatory flows.

A traditional numerical simulation approach is the two-fluid model (Cheng and Hsu, 2014; Hanes and Bowen, 1985; Hsu et al., 2004; Jenkins and Hanes, 1998; Malarkey et al., 2009), in which both the fluid and particle phases are described as inter-penetrating continuum. This approach does not capture the motion of individual sediment particle but solves the concentration field of the particles. To model the inter-particle collision, constitutive relations based on binary collision assumptions are used (Cheng and Hsu, 2014). The two-fluid model is satisfactory in capturing the sediment concentration and sediment flux compared to the experimental results (Cheng and Hsu, 2014; Malarkey et al., 2009). However, since two-fluid models rely on constitutive relations of the particle phase based on binary collisions, it is only valid in relatively dilute flows. In dense flows, the particles have endured contact, and thus the binary collisions may not be applicable (Hou et al., 2012; O’Sullivan, 2011).

CFD–DEM (Computational Fluid Dynamics–Discrete Element Method) is another numerical approach that has been applied to study sediment transport in sheet flows. In contrast to the two-fluid model, CFD–DEM models the motion of sediment particles explicitly, and accounts for the collision of sediment particles. However, due to the limitation of the computational costs, the study of sediment transport in oscillatory flows using CFD–DEM was simplified in the early studies (Calantoni et al., 2004; Drake and Calantoni, 2001). The oscillatory flow was modeled as two-dimensional layers and only a few thousand particles were used. In addition, the early studies

did not resolve the instantaneous turbulent flow and only investigated the mechanics of very coarse sediment particles in oscillatory sheet-flow. With the growth of available computational resources, this approach has gained more popularity in solving sediment transport problems. In the recent works (Schmeeckle, 2014; Sun and Xiao, 2016a), the motion of medium or coarse sand particles in turbulent flows is captured.

1.2. Granular Micromechanics

The granular micromechanics of particle-laden flow are critical in the physical understanding of granular microscopic structures, especially for chemical and pharmaceutical engineering problems (Hou et al., 2012; Kuang and Yu, 2011). The micromechanic variables, including Voronoi volume fraction, coordination number, contact force and others quantities, are obtained based on the packing of the particles. Since such micromechanic variables are much easier to produce from DEM than measuring from experiment, DEM has been extensively used to investigate the granular micromechanics in the past decade (Yi et al., 2011).

DEM has been widely applied to investigate the granular micromechanics in engineering applications, for example, hopper, rotating drum, and sand piles (Langston et al., 1995; Yang et al., 2003; Zhao and Shan, 2013). Micromechanic variables are investigated to understand the heat conduction, particle agglomeration and structural stability. CFD-DEM simulations of pneumatic convey and fluidized bed problems are also performed to study the variation of micromechanic variables in different flow regimes (Hou et al., 2012; Kuang and Yu, 2011). Moreover, the constitutive models are proposed according to the micromechanics of the granular materials (Sun and Sundaresan, 2011), which contributes to macroscopic modeling. Previous studies of granular micromechanics have demonstrated that the CFD-DEM approach has good potential for the granular micromechanics in geotechnical engineering, for example, the modeling of arbitrary-shaped particles (O’Sullivan, 2011). However, the study in granular micromechanics of sediment transport is still lacking.

Although recent studies prove that CFD-DEM is capable of predicting sediment transport in unidirectional turbulent flow (Kidanemariam and Uhlmann, 2014; Schmeeckle, 2014; Sun and Xiao, 2016a), the capability of this approach in predicting the motion of coarse and medium sand in oscillatory flow is still not demonstrated. The present work aims at (1) demonstrating that CFD-

DEM is capable of predicting the instantaneous motion of sediment particles in oscillatory sheet-flow, and (2) investigating the granular micromechanics in sediment transport process. Coarse and medium sands are used in the present numerical simulations. The instantaneous turbulent flow field within the boundary layer is resolved.

The rest of the paper is organized as follows. The methodology of the present model is introduced in Section 2, including the mathematical formulation of fluid equations, the particle motion equations, the fluid–particle interactions, and diffusion-based averaging procedure. The implementation of the code and the numerical methods used in the simulations are detailed in Section 3. In Section 4, the results obtained in the simulations are discussed. Finally, Section 5 concludes the paper.

2. Methodology

2.1. Mathematical Model of Particle Motion

In *SediFoam*, the translational and rotational motions of each particle are calculated based on Newton’s second law as the following equations (Ball and Melrose, 1997; Cundall and Strack, 1979):

$$m \frac{d\mathbf{u}}{dt} = \mathbf{f}^{col} + \mathbf{f}^{fp} + m\mathbf{g}, \quad (1a)$$

$$I \frac{d\mathbf{\Psi}}{dt} = \mathbf{T}^{col} + \mathbf{T}^{fp}, \quad (1b)$$

where \mathbf{u} is the velocity of the particle; t is time; m is particle mass; \mathbf{f}^{col} represents the contact forces due to particle–particle or particle–wall collisions; \mathbf{f}^{fp} denotes fluid–particle interaction forces; \mathbf{g} is body force. I and $\mathbf{\Psi}$ are angular moment of inertia and angular velocity of the particle; \mathbf{T}^{col} and \mathbf{T}^{fp} are the torques due to contact forces and fluid–particle interactions, respectively. To compute the collision forces and torques, the particles are modeled as soft spheres with inter-particle contact represented by an elastic spring and a viscous dashpot. Further details can be found in the study by Tsuji et al. (1993).

2.2. Locally-Averaged Navier–Stokes Equations for Fluids

The fluid flow is described by the locally-averaged incompressible Navier–Stokes equations. Assuming constant fluid density ρ_f , the governing equations for the fluid are (Anderson and Jackson, 1967; Kafui et al., 2002):

$$\nabla \cdot (\varepsilon_s \mathbf{U}_s + \varepsilon_f \mathbf{U}_f) = 0, \quad (2a)$$

$$\frac{\partial (\varepsilon_f \mathbf{U}_f)}{\partial t} + \nabla \cdot (\varepsilon_f \mathbf{U}_f \mathbf{U}_f) = \frac{1}{\rho_f} (-\nabla p + \varepsilon_f \nabla \cdot \mathbf{R} + \varepsilon_f \rho_f \mathbf{g} + \mathbf{F}^{fp}), \quad (2b)$$

where ε_s is the solid volume fraction, $\varepsilon_f = 1 - \varepsilon_s$ is the fluid volume fraction, and \mathbf{U}_f is the fluid velocity. The terms on the right hand side of the momentum equation are: pressure (p) gradient, divergence of the stress tensor \mathbf{R} (including viscous and Reynolds stresses), gravity, and fluid–particle interactions forces, respectively. In the present study, we used large-eddy simulation to resolve the flow turbulence in the computational domain. The stress tensor is composed of both viscous and Reynolds stresses: $\mathbf{R} = \mu \nabla \mathbf{U}_f + \rho_f \mathcal{T}$, where μ is the dynamic viscosity of the fluid flow and \mathcal{T} is the Reynolds stress. The expression of the Reynolds stress is:

$$\mathcal{T} = \frac{2}{\rho_f} \mu_t \mathbf{S} - \frac{2}{3} k \mathbf{I}, \quad (3)$$

where μ_t is the dynamics eddy viscosity, $\mathbf{S} = (\nabla \mathbf{U}_f + (\nabla \mathbf{U}_f)^T)/2$, and k is the turbulent kinetic energy. It is noted that in the stress tensor \mathbf{R} term, the fluctuations of the fluid flow at the boundary of the particle are not resolved. We applied the one-equation eddy viscosity model proposed by Yoshizawa and Horiuti (1985) as the sub-grid scale (SGS) model. This model is selected because it is proven to be adequate to simulate the turbulent flow in a channel (Horiuti, 1985), and it is widely used in large-eddy simulations based on OpenFOAM. In addition, Yoshizawa and Horiuti (1985) observed that the standard Smagorinsky model would be recovered from this model if production equals dissipation in the SGS kinetic energy equation.

2.3. Fluid–Particle Interactions

The fluid-particle interaction force \mathbf{F}^{fp} consists of buoyancy \mathbf{F}^{buoy} , drag \mathbf{F}^{drag} , and lift force \mathbf{F}^{lift} . The drag on an individual particle i is formulated as:

$$\mathbf{f}_i^{drag} = \frac{V_{p,i}}{\varepsilon_{f,i} \varepsilon_{s,i}} \beta_i (\mathbf{u}_{p,i} - \mathbf{U}_{f,i}), \quad (4)$$

where subscripts p and f indicate particle and fluid quantities; $V_{p,i}$ and $\mathbf{u}_{p,i}$ are the volume and the velocity of particle i , respectively; $\mathbf{U}_{f,i}$ is the fluid velocity interpolated to the center of particle i ; β_i is the drag correlation coefficient which accounts for the presence of other particles. The β_i value for the drag force is based on Syamlal et al. (1993):

$$\beta_i = \frac{3}{4} \frac{C_d \rho_f |\mathbf{u}_{p,i} - \mathbf{U}_{f,i}|}{V_r^2 d_{p,i}}, \quad \text{with} \quad C_d = \left(0.63 + 0.48 \sqrt{V_r / \text{Re}}\right), \quad (5)$$

where the particle Reynolds number Re is defined as:

$$\text{Re} = \rho_i d_{p,i} |\mathbf{u}_{p,i} - \mathbf{U}_{f,i}|, \quad (6)$$

the V_r is the correlation term:

$$V_r = 0.5 \left(A_1 - 0.06 \text{Re} + \sqrt{(0.06 \text{Re})^2 + 0.12 \text{Re} (2A_2 - A_1) + A_1^2} \right), \quad (7)$$

with

$$A_1 = \varepsilon_f^{4.14}, \quad A_2 = \begin{cases} 0.8 \varepsilon_f^{1.28} & \text{if } \varepsilon_f \leq 0.85, \\ \varepsilon_f^{2.65} & \text{if } \varepsilon_f > 0.85. \end{cases} \quad (8)$$

The lift force on a spherical particle is modeled in *SediFoam* as (Saffman, 1965; van Rijn, 1984):

$$\mathbf{f}_i^{\text{lift}} = C_l \rho_f \nu^{0.5} D^2 (\mathbf{u}_{p,i} - \mathbf{U}_{f,i}) \times \nabla \mathbf{U}_{f,i}, \quad (9)$$

where \times indicates the cross product of two vectors, and $C_l = 1.6$ is the lift coefficient. In the present study, the Basset history force and added mass force are not considered. The calculation of Basset history force requires the integral of the effect of fluid flow on the particle. Therefore, this would increase the computational resources significantly. For the added mass force, we observed that the simulation would be numerically unstable when the numbers of the layers of sediment particles are large. Hence, the added mass force is not considered in the present simulations.

2.4. Diffusion-Based Averaging

The Eulerian fields ε_s , \mathbf{U}_s , and \mathbf{F}^{fp} in Eq. (2) are obtained by averaging the information of Lagrangian particles. The diffusion equations are used to obtain the continuum Eulerian fields of ε_s ,

\mathbf{U}_s , and \mathbf{F}^{fp} by averaging the discrete particle data. The merits of the diffusion-based averaging approach include (1) sound theoretical foundation, (2) unified treatment of interior and near-boundary particles, (3) guaranteed conservation of relevant physical quantities, (4) easy implementation in CFD solvers with arbitrary meshes, and (5) easy parallelization. Here, the averaging process of ε_s is discussed as an example. In the first step, the particle volumes at each CFD cell are obtained. Then, the solid volume fraction for cell k is calculated by dividing the total particle volume by the volume of this cell $V_{c,k}$:

$$\varepsilon_{s,k}(\mathbf{x}, \tau = 0) = \frac{\sum_{i=1}^{n_{p,k}} V_{p,i}}{V_{c,k}}, \quad (10)$$

where $n_{p,k}$ is the number of particles in cell k . With the initial condition in Eq. (10), a diffusion equation for $\varepsilon_s(\mathbf{x}, \tau)$ is solved to obtain the continuum Eulerian field of ε_s :

$$\frac{\partial \varepsilon_s}{\partial \tau} = \nabla^2 \varepsilon_s \quad (11)$$

where ∇^2 is the Laplacian operator and τ is pseudo-time. It has been established in our previous work (Sun and Xiao, 2015a,b) that the results obtained by Eq. (11) are equivalent with Gaussian kernel based averaging with bandwidth $b = \sqrt{4\tau}$. Similarly, the smoothed \mathbf{U}_s and \mathbf{F}^{fp} fields can be obtained by using this approach.

3. Implementations and Numerical Methods

The hybrid CFD–DEM solver *SediFoam* is developed based on two state-of-the-art open-source codes in their respective fields, i.e., a CFD platform OpenFOAM (Open Field Operation and Manipulation) developed by OpenCFD (2013) and a molecular dynamics simulator LAMMPS (Large-scale Atomic/Molecular Massively Parallel Simulator) developed at the Sandia National Laboratories (Plimpton, 1995). At each time step, the fluid and particle equations are solved individually by the CFD and DEM module. Before solving the fluid equations, the information of the sediment particles from the DEM module is transferred to the CFD module. Then, an averaging procedure is performed to ensure the smoothness of the Eulerian fields reconstructed based on the information of Lagrangian particles. After solving the fluid equations, the fluid-particle interaction force of each particle is updated. Then the DEM module evolves the motion of Lagrangian particles. An interface

is implemented for OpenFOAM and LAMMPS to transfer the particle information based on Open-MPI. The code is open-source and is available at <https://github.com/xiaoh/sediFoam>. Detailed information of the implementations is discussed in our previous paper (Sun and Xiao, 2016b).

It should be noted that the open-source solver *CFDEM* is also a coupled solver of OpenFOAM and LAMMPS (Goniva et al., 2009; Schmeekle, 2014). However, *SediFoam* focuses on sediment transport problems with several features:

1. The volume fraction terms are not considered in sediment transport applications in *CFDEM* (Furbish and Schmeekle, 2013; Schmeekle, 2014); whereas *SediFoam* first considered the volume fraction terms. Since these terms are considered in *SediFoam*, the mass conservation is guaranteed. This is because *SediFoam* uses the diffusion-based averaging algorithm and can obtain smooth Eulerian fields from Lagrangian particles on arbitrary meshes.
2. Pressure gradient force, fluid viscous force, lift force, lubrication force and added mass force, which are not negligible in sediment transport applications, are implemented in *SediFoam*. However, in *CFDEM*, only pressure gradient force and fluid viscous forces are considered.
3. The parallel efficiency of *SediFoam* is very good when using up to 512 processors on simulations of 40 million sediment particles. This is because the parallel efficiency of the interface between OpenFOAM and LAMMPS is satisfactory.

The fluid equations in (2) are solved in OpenFOAM with the finite volume method (Jasak, 1996). PISO (Pressure Implicit Splitting Operation) algorithm is used to prevent velocity–pressure decoupling (Issa, 1986). A second-order central scheme is used for the spatial discretization of convection terms and diffusion terms. Time integrations are performed with a second-order implicit scheme. In the averaging procedure, the diffusion equations are solved on the same mesh as the CFD mesh (Capecelatro and Desjardins, 2013; Sun and Xiao, 2015b). A second-order central scheme is used for the spatial discretization of the diffusion equation; a second-order implicit scheme is used for the temporal integration. To model the collision between the sediment particles, the contact force between sediment particles is computed with a linear spring-dashpot model. In this model, the normal push-back force for two overlapping particles is linearly proportional to the overlap distance; the damping force is proportional to the relative velocity between two overlapping particles (Cundall

and Strack, 1979). This linear spring-dashpot model is proven to be adequate in the simulation of particle-laden flows (Gupta, 2015; Kidanemariam and Uhlmann, 2014).

4. Results

Setups of the numerical simulations performed here follow the experimental study of sediment transport in an asymmetric oscillatory flow (O’Donoghue and Wright, 2004a,b). The purposes of the numerical simulations are (1) to validate the capability of the CFD–DEM model under oscillatory flow actions, and (2) to reveal the physical insights of the variation of micromechanic variables at different phases in the oscillatory flow cycle. In Section 4.1, the results obtained in the numerical simulations are compared to the experimental results, which aims to demonstrate that CFD–DEM is capable of predicting the sediment transport in oscillatory sheet-flows. In Section 4.2, the study of the micromechanics of sediment bed is detailed. The Voronoi volume fraction, the coordination number, and the inter-particle contact force are presented, which aims to compare the micromechanics of sediment bed at different phases. In addition, the effect of the particle size on these micromechanic variables is demonstrated.

4.1. Numerical validation

The numerical tests are performed using a periodic channel according to the literature (Malarkey et al., 2009; O’Donoghue and Wright, 2004a,b). The geometry of the computational domain and the coordinates system are shown in Figure 1. The Cartesian coordinates x , y , and z are aligned with the streamwise, vertical, and lateral directions, respectively. The boundary conditions in both x - and z -directions are periodic. The no-slip wall boundary condition is applied at the bottom while free-slip condition is applied on the top. The three fixed layers are arranged in hexagonal packing according to (Kempe et al., 2014). Since the velocity of the particles at the bottom is very small, the pattern of the fixed particle does not significantly influence the results. The CFD mesh is refined in the vertical (y -) direction at the particle-fluid interface to resolve the flow structure in the boundary layer. The top of the initial bed corresponds to $y = 0$. The physical parameters used are detailed in Table 1. Based on previous studies on sediment transport in unidirectional flow using CFD–DEM (Furbish and Schmeeckle, 2013; Schmeeckle, 2014), the size of the computational

domain is chosen to be $100\text{--}240d_p$ in streamwise direction and $60\text{--}120d_p$ in lateral direction. Since the size of the computational domain in the present study is within the range of previous studies (see Table 1), the computational domain used is adequate. In addition, the numbers of sediment particles range from 24,000 to 330,000 in previous tests in unidirectional flow (Furbish and Schmeeckle, 2013; Schmeeckle, 2014). Since the numbers of sediment particles in the present study are 256,000 and 108,000, the numbers of sediment particle are also adequate. It should be noted that the mesh resolutions are different in the cases because the diameters of the particles used are different. In the present simulations, the sediment particles are arranged in hexagonal lattice, and the size of the CFD mesh is $2d_p/\sqrt{3}$ in streamwise direction and $2d_p$ in lateral direction. This is to avoid the variation of solid volume fraction ε_s on the bottom CFD cells for the uniform distributed bottom particles. Since the computational domains in the cases are similar (although not consistent), the mesh resolutions are different. From mesh-independent study by Schmeeckle (2014), the mesh resolution in the present study is adequate to resolve the turbulent eddies at the boundary layer. The experimental measurements are performed using coarse, medium and fine sands. In this work, we focus on the simulations of coarse and medium sands. The simulation of fine sand case is not performed because the computational costs are unaffordable when the erosion depth is approximately $100d_p$. The height of the domain in the numerical simulation is 75 mm, which is smaller than the channel height 750 mm in the experiment. This reduction of the computational domain is to limit the computational costs. It is noted that the sediment particle used in the experiment is well-sorted, but uniform-sized particles are used in the present simulations. This is because the detailed particle size distribution is not given. Moreover, the results obtained in previous studies using uniform-sized particle are satisfactory (Malarkey et al., 2009).

The stiffness, the restitution coefficient, and the friction coefficient are also detailed in Table 1. In the present simulations, the restitution coefficient e is 0.01 according to Schmeeckle (2014), which is smaller than that used by Drake and Calantoni (2001). This is due to the fact that the effective restitution coefficient of coarse and medium particles (Stokes number < 10) in water is very small when the lubrication layer is formed between the contact particles (Kempe and Fröhlich, 2012). The selection of the friction coefficient in the present study according to Kidanemariam and Uhlmann

(2014). However, the results are not sensitive to the restitution coefficient and friction coefficient in the present simulations. The typical contact time is 4.6×10^{-4} s for coarse sand and 2.0×10^{-4} s for medium sand. The DEM step in the present study is 2.0×10^{-6} s, which is smaller than 1/50 of the contact time to avoid particle inter-penetration (Sun et al., 2007).

The asymmetric sheet flow velocity is shown in Figure 2. The time history of this oscillatory flow is:

$$u(t) = u_1 \sin(\omega t) - u_2 \cos(2\omega t), \quad (12)$$

where $\omega = 2\pi/T$; u_1 and u_2 determine the magnitude and asymmetry of the wave, respectively. According to O'Donoghue and Wright (2004b), when the flow velocity is positive, it is onshore-directed; whereas the flow is offshore-directed when the velocity is negative. This second order Stokes wave is typical of natural surf zone in the production of sediment transport (Drake and Calantoni, 2001). The fluid flow is driven by an oscillatory pressure gradient $p_d(t)$, which is the time derivative of flow velocity:

$$p_d(t) = u_1 \omega \cos(\omega t) + 2u_2 \omega \sin(2\omega t). \quad (13)$$

The flow velocity and sediment flux obtained in the present simulation are validated by using the experimental data at different phases of the oscillatory flow cycle, which are indicated as the vertical line in Figure 2.

The profiles of horizontally averaged flow velocity in the streamwise direction obtained in the present simulations are shown in Figure 3. It can be seen in the figure that the flow velocity profiles obtained by using CFD-DEM agree with the experimental data at all the phases examined in the oscillatory cycle. The height of the computational domain is smaller than that in the experiment, but it is sufficient to capture the bulk physics of the fluid flow. In addition to the flow velocity, the sediment flux is also examined to validate the numerical simulation. The sediment flux φ is defined as $\varphi = \varepsilon_s U_{f,x}$, where $U_{f,x}$ is the streamwise component of the fluid velocity. Although the particle velocity $U_{s,x}$ should be used in the definition of sediment flux (Schmeeckle, 2014), the present study uses the fluid velocity $U_{f,x}$ to be consistent with the definition in the experimental studies (O'Donoghue and Wright, 2004a,b). This is attributed to the fact that the particle velocity

is difficult to measure in the oscillatory flow experiment, and thus the fluid velocity is used instead. Considering the terminal velocity of the sediment particle is very small compared with the flow velocity, the differences between horizontally averaged fluid velocity and particle velocity are not significant.

Figure 4 shows that the vertical profiles of sediment flux obtained from the numerical simulations are consistent with the experiment results. When measuring high concentration regions in the experiments, CCM probes can only be applied at the bottom (concentration higher than 6%, which is located within 2 mm above the initial sediment bed) to provide good concentration measurements. To measure low concentration regions, the suction samplers can produce a significant lowering of the mean bed level (from 10 to 30 mm) in their vicinity, and thus are located approximately 10 mm above the bed to reduce its influence on the seabed ($h > 10$ mm). Because of the limitations of the experimental measurements, there is a gap of the order of 10 mm profiles of sediment flux. It can be seen in Figure 4 that the agreement between the experimental results and numerical simulation is satisfactory for both regions measured by CCM probes and suction samplers. The discrepancy between the results obtained in the experiments and numerical simulations is attributed to the uncertainty of the measurement and numerical model. The gap in the experimental measurement is bridged since the concentration and velocity of the moving particles are easier to obtain in the simulations. This is an advantage of the CFD–DEM approach over the experimental measurement. Based on the sediment flux obtained in the simulations, the particles on the surface of the sediment bed are moving with fluid flow, but those on the bottom are almost stationary. When the particle number increases in the simulations, only the number of non-moving particle is increasing and the results are not sensitive to the number of particles. This shows the number of sediment particles is sufficient in the present simulations.

Another quantity of interest is the transport rate of the sediment particles, which is defined as the spacial integral of the sediment flux at the sheet flow layer:

$$q_{sf} = \int_{-\sigma_e}^{y_s} \varphi dy, \quad (14)$$

where σ_e is the height of the erosion depth; y_s is the height of the sheet flow layer. According to O’Donoghue and Wright (2004a), the erosion depth is defined according to a 2-step procedure:

Table 1: Parameters used in numerical simulations of sediment transport.

	Case 1 (medium sand)	Case 2 (coarse sand)
bed dimensions		
width (L_x)	$139d_p$ (37.4 (mm))	$104d_p$ (47.8 (mm))
height (L_y)	$278d_p$ (75 (mm))	$163d_p$ (75 (mm))
transverse thickness (L_z)	$80d_p$ (21.6 (mm))	$60d_p$ (27.6 (mm))
mesh resolutions		
width (N_x)	80	60
height (N_y)	180	180
transverse thickness (N_z)	40	30
particle properties		
total number	256,000	108,000
diameter d_p	0.27 (mm)	0.46 (mm)
density ρ_s	2.65×10^3 (kg/m ³)	
particle stiffness coefficient	20 (N/m)	
normal restitution coefficient	0.01	
coefficient of friction	0.4	
fluid properties		
density ρ_f	1.0×10^3 (kg/m ³)	
kinetic viscosity ν	1.0×10^{-6} (m ² /s)	
wave properties (see Eq. (12))		
u_1	1.06 (m/s)	
u_2	0.22 (m/s)	
period (T)	5.0 (s)	

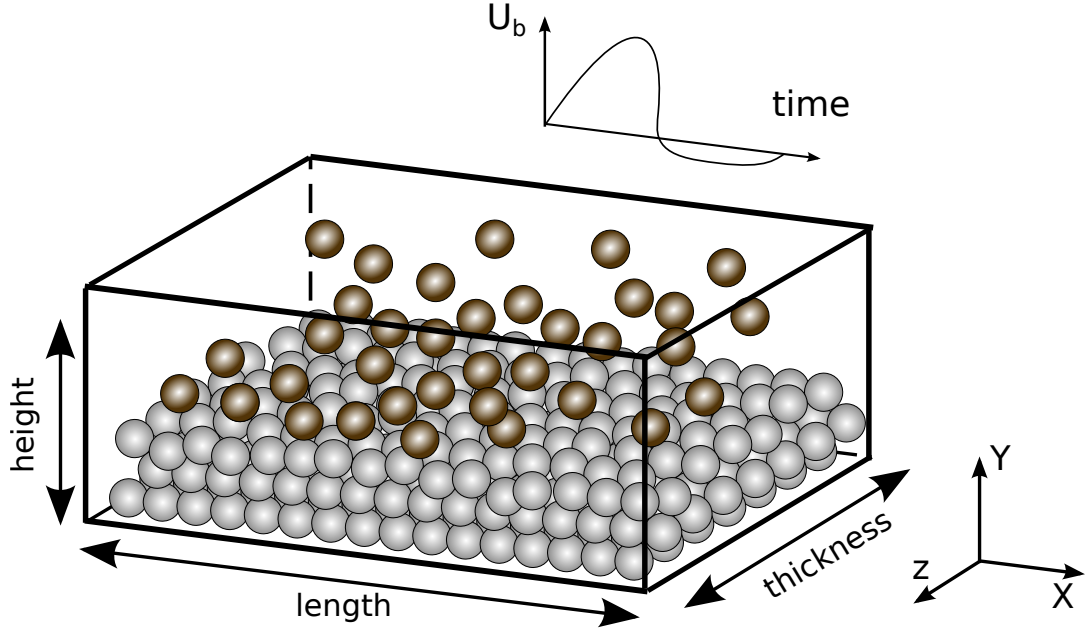


Figure 1: The geometry of the computational domain in the numerical simulations. The grey “immobile” particles are fixed at the bottom; the brown particles are movable. For clarity, only a few mobile particles are shown here for illustration purpose. The simulations used 250,000 and 108,000 particles. The particle sizes are not to scale.

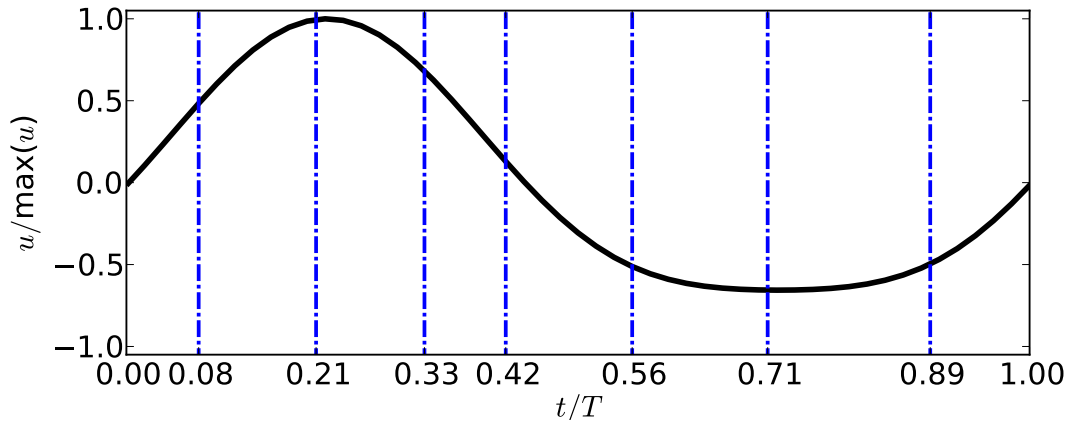


Figure 2: Time history of the mean flow velocity. Vertical lines indicate eight phases at which the results obtained from the numerical simulations are compared to the experiments.

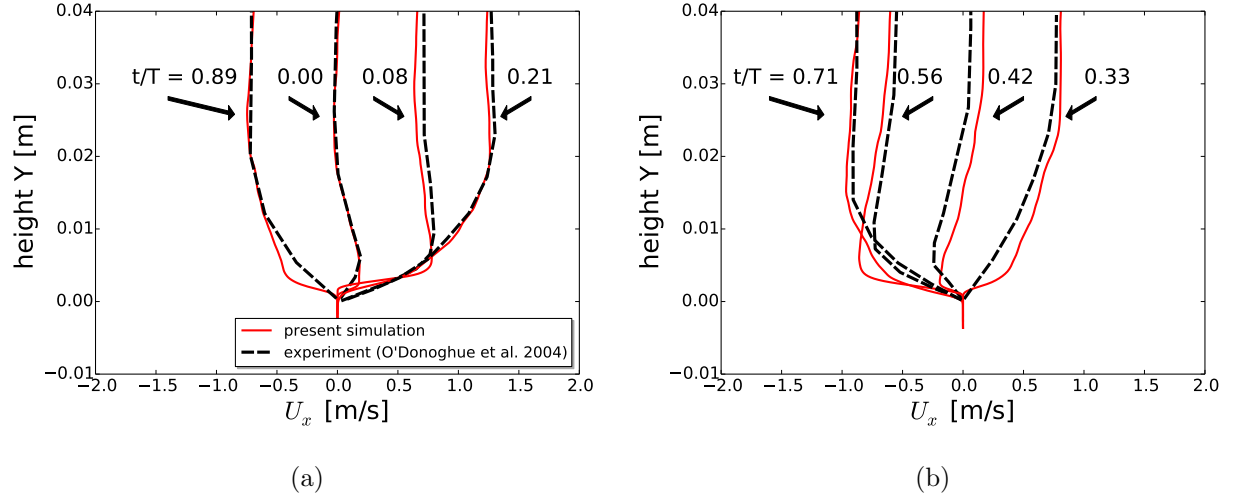


Figure 3: Horizontally-averaged streamwise flow velocity for Case 1 at different phases in the oscillatory flow cycle. To show each velocity profile clearly, the profiles are split according to Figure 6 in O'Donoghue and Wright (2004b).

(1) find the vertical concentration profile of best fit; (2) draw a tangent line from the inflection point on the profile, and find the point of intersection between the concentration profile and $\varepsilon_s = 0.6$. However, in the present study, the sediment flux at the bottom is very small and the integral in Eq. (14) starts from the bottom of the computational domain. The height of the sheet flow layer is defined at the location where $\varepsilon_s = 0.08$. The sediment transport rates q_{sf} obtained in the CFD–DEM simulations are compared with the experimental results for Cases 1 and 2. It can be seen in Figure 5 that the sediment transport rates obtained in the CFD–DEM simulations are consistent with the experimental data in both cases. CFD–DEM captures the peak at $t/T = 0.21$ and the trough of the sediment transport rate, which demonstrates the capability of CFD–DEM in the prediction of both onshore and offshore sediment transport. The time integral of the transport rate in one period is the net sediment transport rate, which can be used to evaluate the rate of onshore and offshore sediment transport. The net sediment transport rates of the two cases are 53 and 44 mm^2/s , which agree very well with the experimental measurement of 56 and 45 mm^2/s (Malarkey et al., 2009). According to the results, the asymmetric wave leads to net onshore sediment transport

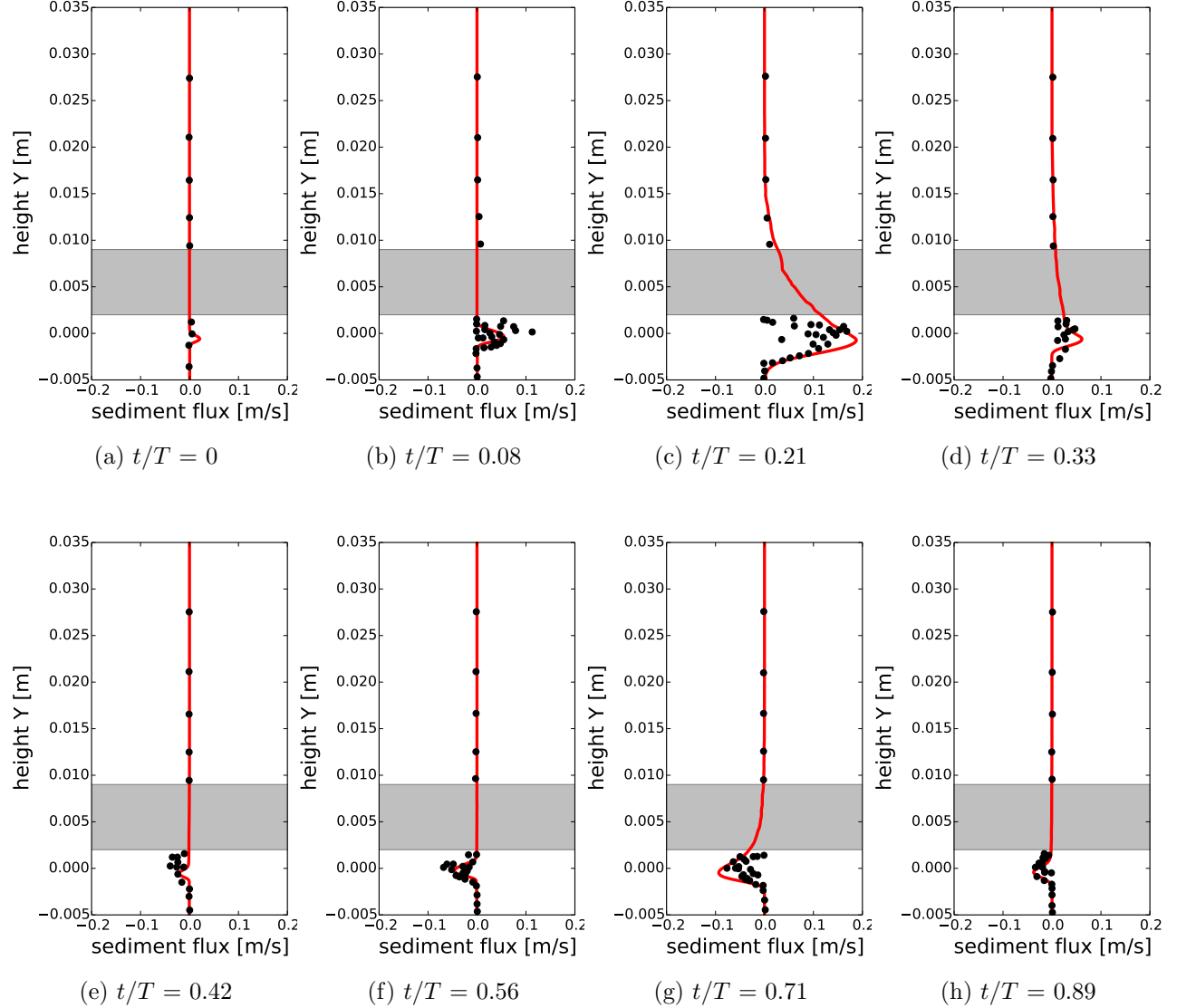


Figure 4: Horizontally-averaged streamwise sediment flux for Case 1 at different phases. The red solid lines are the results obtained by using CFD-DEM; the black dots are the experimental measurements. It is noted that there is a gap (highlighted in shade) in the experimental data between conductivity concentration probes ($h < 2$ mm) and suction samplers ($h > 10$ mm). The initial surface of the sediment bed is $y = 0$.

for both cases.

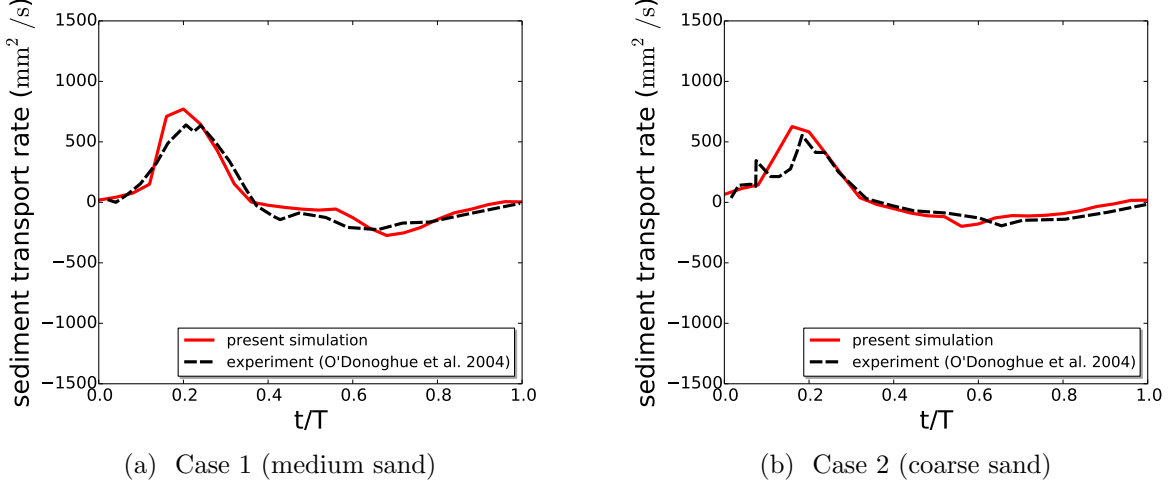


Figure 5: Time-hisotry of the oscillatory sheet-flow sediment transport rate for Cases 1 and 2.

In summary, the overall agreement between the results obtained by the numerical simulation and experimental measurement is satisfactory in general. This indicates that the CFD–DEM model is capable of predicting the sediment flux in oscillatory flows.

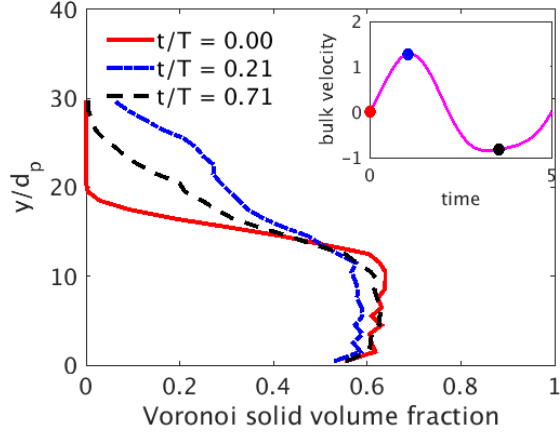
4.2. Granular Micromechanics

The micromechanic variables at different phases in the oscillatory cycle of both cases are compared, including the Voronoi volume fraction, the coordination number, and the contact force. The volume fraction and coordination number describe the packing of sediment bed; the total contact force indicates the particle interaction. For each sediment particle, the Voronoi volume fraction is the ratio of the volume of this particle and the total volume this particle occupies; the coordination number is the number of contact from neighboring particles; the total contact force is the resultant of the contact force from neighboring particles. The purpose of the comparison of micromechanic variables is to demonstrate the evolution of sediment bed in oscillatory flows. Detailed definitions of the micromechanic variables and post-processing procedures are discussed in the Appendix.

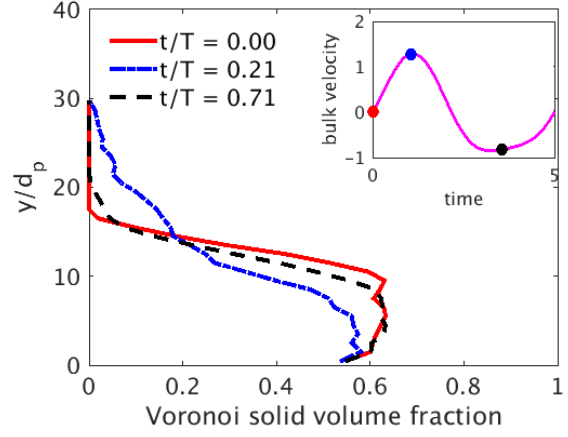
The horizontally averaged profiles of Voronoi volume fraction at three representative phases in the oscillatory sheet-flow are shown in Figures 6(a) and (b). For both medium and coarse

sands, the Voronoi volume fractions at the phases corresponding to the maximum onshore/offshore sediment fluxes ($t/T = 0.21$ and 0.71) are more diffusive than the phases corresponding to the minimum sediment flux ($t/T = 0.00$). Here, diffusive means the gradient of the micromechanic variable is smaller. The Voronoi volume fraction becomes diffusive because the mixing of solid phase and fluid phase at large fluid velocities. In addition, the sediment particles occupy more space when suspended in the flow. The Voronoi volume fraction profile at the maximum onshore-directed fluid flux ($t/T = 0.21$) is more diffusive than that at the maximum offshore-directed fluid flux ($t/T = 0.71$). This can be attributed to the fact that the number of suspended particles is larger when the onshore-directed flow velocity is larger than the offshore-directed flow velocity. In addition, the Voronoi volume fraction for coarse sand is less diffusive than medium sand at the phases corresponding to the maximum onshore/offshore sediment fluxes. This is because the inertia of coarse particles is larger and they are less likely to become suspended. The probability density functions of distribution of Voronoi volume fraction are also used to demonstrate the validation of micromechanic variables in Figures 6(c) and (d). It can be seen that the peaks of the probability density function for the sediment bed corresponding to the minimum fluid flux ($t/T = 0.00$) in both cases are at $\varepsilon_s = 0.62$, which is consistent with the volume fraction for poured random packing (Dullien, 1979). When the fluid flux increases, the sediment particles on the bed become suspended and occupy more space. Hence, more particles have larger Voronoi cells, and fewer particles are closely packed. Therefore, the peak value in the probability density function moves leftward and decreases in magnitude.

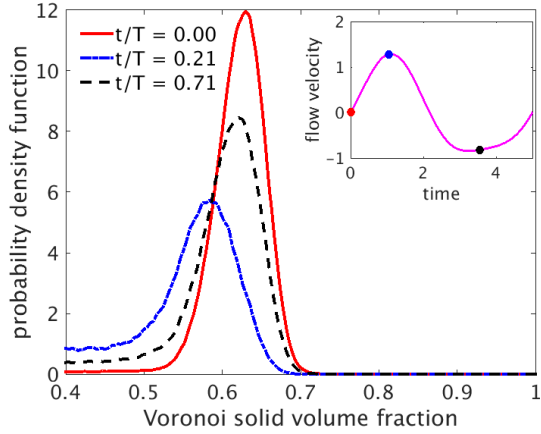
The coordination number (CN) is defined as the number of nearest neighbors of the sediment particle. This quantity is useful in the evaluation of the structural properties of the sediment particles, for example, the packing and permeability of the sediment bed. The horizontally averaged coordination number profiles for Cases 1 and 2 are shown in Figures 7(a) and (b), respectively. It can be seen that the coordination number decreases at the phases corresponding to the maximum onshore/offshore sediment fluxes, which is because the suspended particles have less contact when suspend. Moreover, the probability density functions are shown in Figures 7(c) and (d). The peak of the probability density functions is located at coordination number $CN = 5$ at $t/T = 0.00$, which



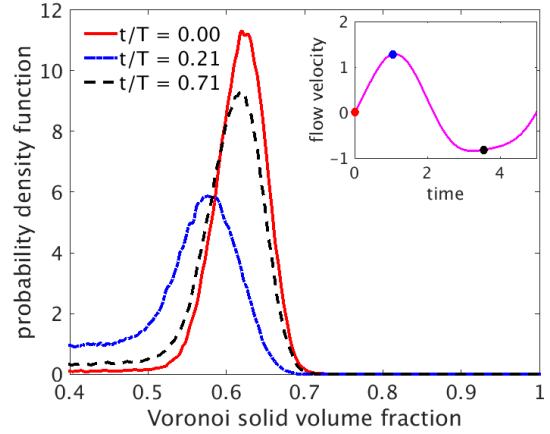
(a) Case 1 (medium sand), vertical profile



(b) Case 2 (coarse sand), vertical profile



(c) Case 1 (medium sand), probability density



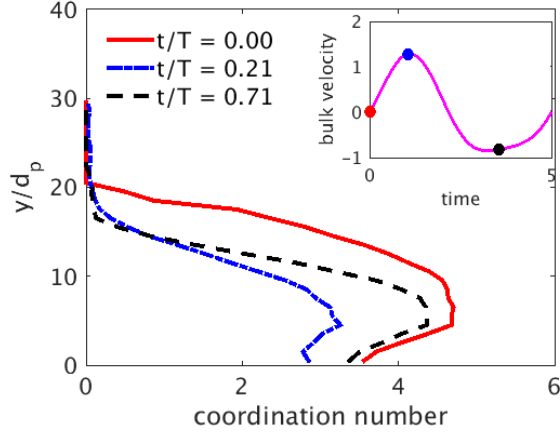
(d) Case 2 (coarse sand), probability density

Figure 6: The horizontally-averaged vertical profiles and probability density functions of Voronoi volume fraction of Cases 1 and 2 at three representative phases: (1) $t/T = 0$, (2) $t/T = 0.21$, and (3) $t/T = 0.71$.

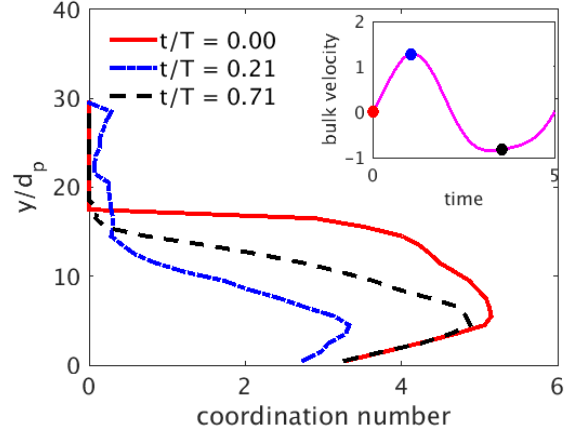
is consistent with results obtained in the DEM simulations of a rotating drum (Yang et al., 2003). Figures 7(c) and (d) also show the variation of the coordination number at different phases in the oscillatory cycle. Similar with those of the volume fraction, the peaks of the probability density move leftward when the sediment transport rate increases. Moreover, a significant increase for the probability density function of the coordination number $CN = 0$ and 1 can be seen in Figures 7(c) and (d), which is due to the suspension of sediment particles. The increase of the probability density of coarse sand is less than that for the medium sand, which is due to the fact that coarse particles are less likely to become suspended. Compared to the prediction of the coordination number by CFD-DEM, the two-fluid model uses binary collision assumptions and the coordination number $CN = 1$ is assumed constant (Cheng and Hsu, 2014). It can be seen from Figures 7(a) and (b) that the coordination number under the sediment bed is much larger than 1 . Therefore, the binary collision assumption underestimates the contact of the sediment particles.

The relationship between the Voronoi volume fraction and the coordination number is shown in Figure 8. The relationship obtained in sediment transport is compared to the results obtained in the CFD-DEM simulations of fluidized bed flow (Hou et al., 2012). It can be seen that at the phase corresponding to minimum fluid flux ($t/T = 0.00$), the correlation of Voronoi volume fraction and coordination number is consistent with the results obtained in fixed bed regime in the fluidized bed flow. At the phases corresponding to the maximum onshore/offshore fluid flux ($t/T = 0.21$ and 0.71), this correlation is consistent with fluidized bed regime. The ratio of coordination number and Voronoi volume fraction of coarse sand is larger than that of medium sand, which indicates that the fraction of fluidized medium sand in the seabed is larger than that of coarse sand. This ratio is even larger when the fluid flow is offshore-directed for coarse sand, which is described as partially-fluidized by Hou et al. (2012). This is because the coarse particles are less likely to move when the offshore-directed fluid flux is relatively small.

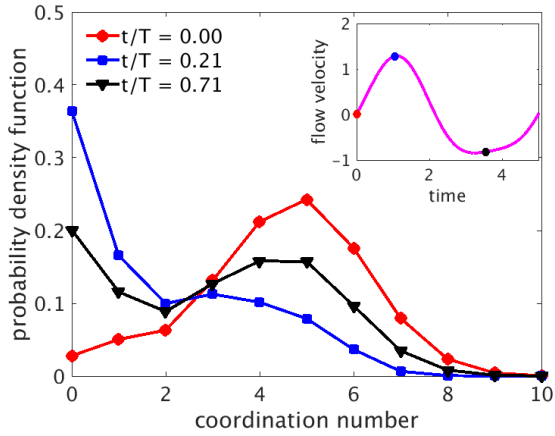
Another micromechanic variable is the normal contact force between sediment particles. Figure 9 shows the probability density functions of the normal contact forces. The contact force is normalised by the weight of the particle. The peaks of the density functions are located approximately at $F_n/mg = 10$, which is consistent with previous DEM simulations of a rotating drum (Yang et al.,



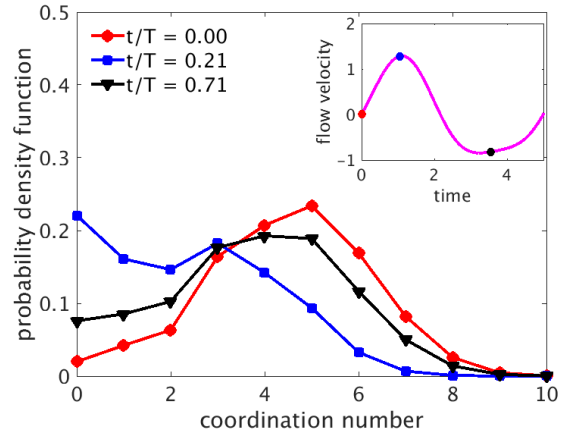
(a) Case 1 (medium sand), vertical profile



(b) Case 2 (coarse sand), vertical profile



(c) Case 1 (medium sand), probability density



(d) Case 2 (coarse sand), probability density

Figure 7: The horizontally-averaged vertical profiles and probability density functions of coordination number of Cases 1 and 2 at three representative phases: (1) $t/T = 0$, (2) $t/T = 0.21$, and (3) $t/T = 0.71$.

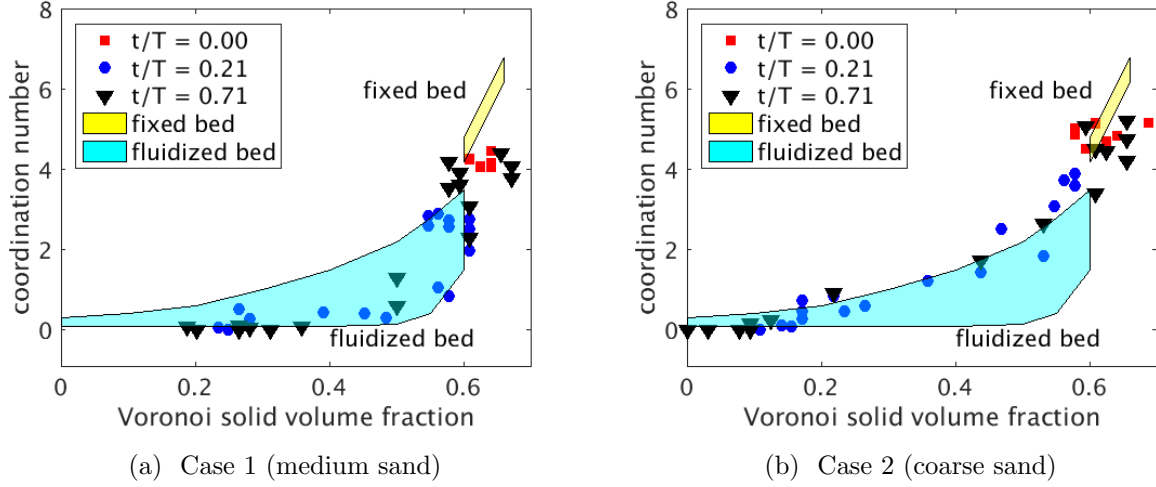


Figure 8: The relationship between the coordination number and Voronoi volume fraction. The shade is obtained from the fluidized bed simulations by Hou et al. (2012).

2003). These peaks of the probability density decrease in magnitude when $t/T = 0.21$ and 0.71 because the particles located near the top become suspended. Since medium sand particles are more likely to become suspended than coarse particles, the decrease of the magnitude of the peak is larger. Figure 9 also shows the increase of the normal contact force when the fluid flux increases. To investigate this increase of the contact force, the contact force network is visualized to determine the force chain formation in the sediment bed, which is shown in Figure 10. The contact force network is the plot of the contact force between contacting particles. The contact force network can illustrate the propagation of the contact force in granular materials. In Figure 10, the color and diameter of the cylinder denote the magnitude of the force. It can be seen in Figure 10 that the contact force for fixed sediment bed increases at the bottom due to the effect of gravity force. On the other hand, for moving sediment bed, the contact force of some suspended particles is large. The suspended particles have larger velocity, and the probability to have large relative velocity between the particles is higher. Therefore, the contact force of some suspended particles is significantly larger than particles rolling and sliding on the sediment bed. It can be also seen in Figures 10(a) and (b) that the contact forces between coarse sand particles are larger than those in medium sand at the

phases that the fluid flux is zero. This can be explained by the fact that when flow flux is zero, most sediment particles are not moving on the sediment bed. Since the relative velocity between fluid and sediment particle is small, the drag force on the sediment particle is small compared to particle weight. In addition, the pressure gradient force is almost equal to the buoyancy force since the flow is stationary. The resultant of the contact forces on each particle balances the particle's submerged weight, which is the sum of gravity and buoyancy. Since the submerged weight of coarse sand is larger than that of medium sand, the inter-particle contact force on coarse sand is larger.

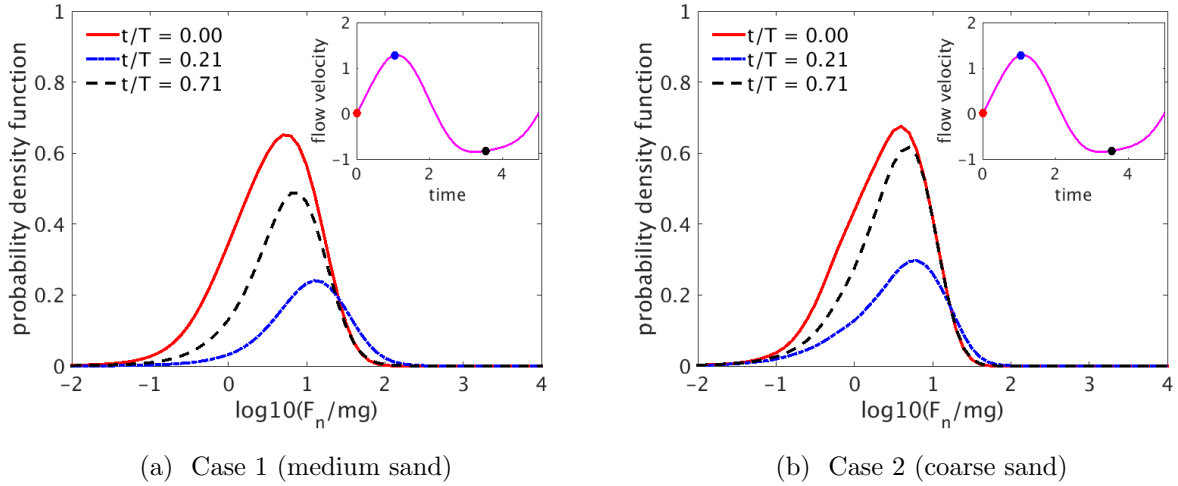
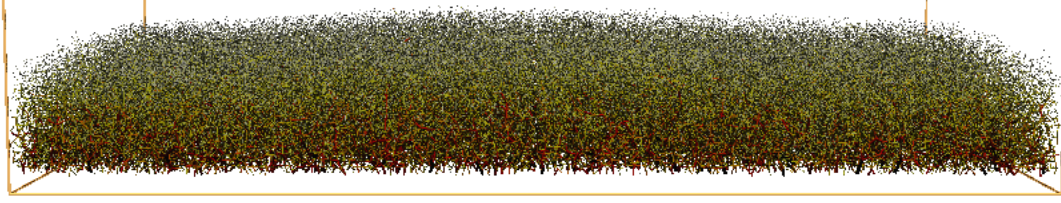


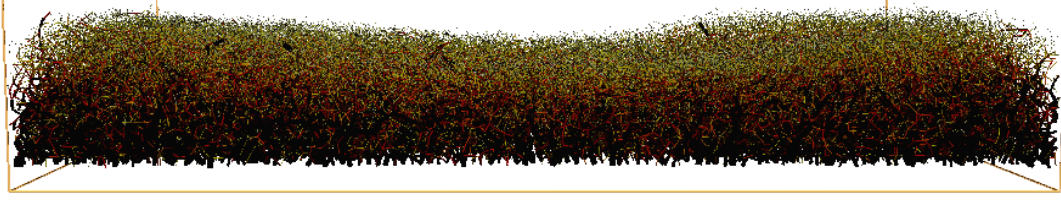
Figure 9: Probability density functions of the contact force at different phases in oscillatory flow for Cases 1 and 2.

5. Conclusion

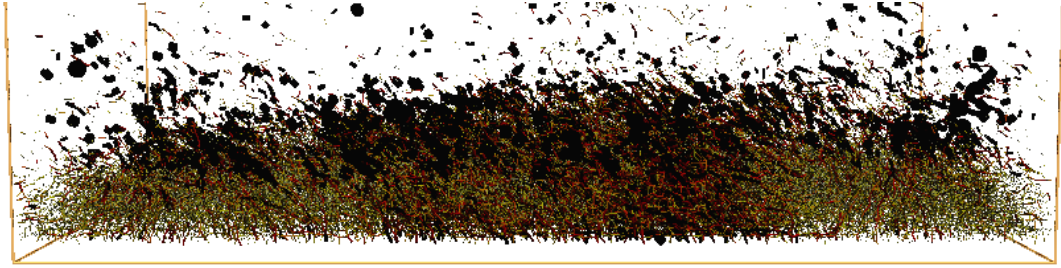
In this work, numerical simulations of sediment transport in oscillatory sheet-flow are performed by using CFD–DEM solver *SediFoam*. The results obtained by using CFD–DEM simulations are compared to the experimental data of coarse and medium sands. The comparisons have demonstrated that predictions of fluid velocity, the sediment flux, and the sediment transport rate are consistent with the experimental measurements at different phases in the oscillatory flow cycle. The consistency between the experimental data and the results from the numerical simulation demon-



(a) Case 1 (medium sand), $t/T = 0$



(b) Case 2 (coarse sand), $t/T = 0$



(c) Case 1 (medium sand), $t/T = 0.21$



(d) Case 2 (coarse sand), $t/T = 0.21$

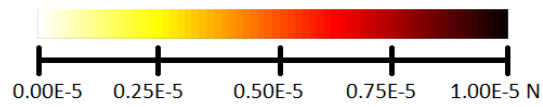


Figure 10: The force network of the sediment transport in oscillatory flow for Cases 1 and 2 at two representative phases in the oscillatory flow cycle: (1) $t/T = 0$ (fixed bed with zero sediment flux); (2) $t/T = 0.21$ (maximum sediment flux). The color and the diameter of the cylinder denote the magnitude of the force.

strate that CFD–DEM is capable of simulating the sediment transport problems in oscillatory flow for coarse and medium sands.

In addition, the micromechanics of sediment bed are studied, including the Voronoi volume fraction, the coordination number, and the particle contact force. It is demonstrated that the behavior of the micromechanic variables varies significantly at different phases in the oscillatory flow, which indicates the microscopic structure of sediment bed is dependent on the fluid flux. Moreover, the micromechanic variables of the sediment bed are similar to the fluidized bed at high sediment transport rate; whereas the variables are similar to the fixed bed at low sediment transport rate. From the prediction of the CFD–DEM model, we observed that the coordination number in rapid sheet flow layer is larger than one, which indicates that a typical particle in the sediment layer is in contact with more than one particles, and thus the binary collision model commonly used in two-fluid model may underestimate the contact between the particles.

6. Acknowledgment

The computational resources used for this project were provided by the Advanced Research Computing (ARC) of Virginia Tech, which is gratefully acknowledged. The authors would like to thank for Dr. Gupta for the code and technical assistance in the post-processing of the granular micromechanics. The authors gratefully acknowledge partial funding of graduate research assistantship from the Institute for Critical Technology and Applied Science (ICTAS, Grant number 175258).

Reference

References

- Anderson, T., Jackson, R., 1967. A fluid mechanical description of fluidized beds: Equations of motion. *Industrial and Chemistry Engineering Fundamentals* 6, 527–534.
- Ball, R. C., Melrose, J. R., 1997. A simulation technique for many spheres in quasi-static motion under frame-invariant pair drag and Brownian forces. *Physica A: Statistical Mechanics and its Applications* 247 (1), 444–472.

- Calantoni, J., Holland, K. T., Drake, T. G., 2004. Modelling sheet-flow sediment transport in wave-bottom boundary layers using discrete-element modelling. *Philosophical Transactions of Royal Society of London: Series A* 362, 1987–2002.
- Capecelatro, J., Desjardins, O., 2013. An Euler–Lagrange strategy for simulating particle-laden flows. *Journal of Computational Physics* 238, 1–31.
- Cheng, Z., Hsu, T.-J., 2014. A turbulence-resolving Eulerian two-phase model for sediment transport. *Coastal Engineering Proceedings* 1 (34), 74.
- Cundall, P., Strack, D., 1979. A discrete numerical model for granular assemblies. *Géotechnique* 29, 47–65.
- Drake, T. G., Calantoni, J., 2001. Discrete particle model for sheet flow sediment transport in the nearshore. *Journal of Geophysical Research: Oceans* (1978–2012) 106 (C9), 19859–19868.
- Dullien, F. A., 1979. *Porous media: fluid transport and pore structure*. Academic press: San Diego, CA.
- Flores, N. Z., Sleath, J., 1998. Mobile layer in oscillatory sheet flow. *Journal of Geophysical Research* 103 (C6), 12783–12793.
- Furbish, D., Schmeeckle, M., 2013. A probabilistic derivation of the exponential-like distribution of bed load particle velocities. *Water Resources Research* 49 (3), 1537–1551.
- Goniva, C., Kloss, C., Pirker, S., 12-13 November 2009. Towards fast parallel CFD–DEM: an open-source perspective. In: *Proc. of Open Source CFD International Conference*.
- Gupta, P., 2015. Verification and validation of a DEM–CFD model and multiscale modelling of cohesive fluidization regimes. Ph.D. thesis, The University of Edinburgh.
- Hanes, D. M., Bowen, A. J., 1985. A granular-fluid model for steady intense bed-load transport. *Journal of Geophysical Research: Oceans* (1978–2012) 90 (C5), 9149–9158.

- Horiuti, K., 1985. Large eddy simulation of turbulent channel flow by one-equation modeling. *Journal of the Physical Society of Japan* 54 (8), 2855–2865.
- Hou, Q., Zhou, Z., Yu, A., 2012. Micromechanical modeling and analysis of different flow regimes in gas fluidization. *Chemical Engineering Science* 84, 449–468.
- Hsu, T.-J., Jenkins, J. T., Liu, P. L.-F., 2004. On two-phase sediment transport: sheet flow of massive particles. In: *Proceedings of the Royal Society of London A: Mathematical, Physical and Engineering Sciences*. Vol. 460. The Royal Society, pp. 2223–2250.
- Issa, R. I., 1986. Solution of the implicitly discretised fluid flow equations by operator-splitting. *Journal of Computational Physics* 62 (1), 40–65.
- Jasak, H., 1996. Error analysis and estimation for the finite volume method with applications to fluid flows. Ph.D. thesis, Imperial College London (University of London).
- Jenkins, J. T., Hanes, D. M., 1998. Collisional sheet flows of sediment driven by a turbulent fluid. *Journal of Fluid Mechanics* 370, 29–52.
- Kafui, K., Thornton, C., Adams, M., 2002. Discrete particle–continuum fluid modelling of gas–solid fluidised beds. *Chemical Engineering Science* 57 (13).
- Kempe, T., Fröhlich, J., 2012. Collision modelling for the interface-resolved simulation of spherical particles in viscous fluids. *Journal of Fluid Mechanics* 709, 445–489.
- Kempe, T., Vowinckel, B., Fröhlich, J., 2014. On the relevance of collision modeling for interface-resolving simulations of sediment transport in open channel flow. *International Journal of Multiphase Flow* 58, 214–235.
- Kidanemariam, A. G., Uhlmann, M., 2014. Direct numerical simulation of pattern formation in subaqueous sediment. *Journal of Fluid Mechanics* 750, R2.
- Kuang, S., Yu, A., 2011. Micromechanic modeling and analysis of the flow regimes in horizontal pneumatic conveying. *AIChE journal* 57 (10), 2708–2725.

- Langston, P. A., Tüzün, U., Heyes, D. M., 1995. Discrete element simulation of granular flow in 2D and 3D hoppers: dependence of discharge rate and wall stress on particle interactions. *Chemical Engineering Science* 50 (6), 967–987.
- Malarkey, J., Pan, S., Li, M., ODonoghue, T., Davies, A., OConnor, B., 2009. Modelling and observation of oscillatory sheet-flow sediment transport. *Ocean Engineering* 36 (11), 873–890.
- O’Donoghue, T., Wright, S., 2004a. Concentrations in oscillatory sheet flow for well sorted and graded sands. *Coastal Engineering* 50 (3), 117–138.
- O’Donoghue, T., Wright, S., 2004b. Flow tunnel measurements of velocities and sand flux in oscillatory sheet flow for well-sorted and graded sands. *Coastal Engineering* 51 (11), 1163–1184.
- OpenCFD, 2013. OpenFOAM User Guide. See also <http://www.opencfd.co.uk/openfoam>.
- O’Sullivan, C., 2011. Particle-based discrete element modeling: Geomechanics perspective. *International Journal of Geomechanics* 11 (6), 449–464.
- Plimpton, J., 1995. Fast parallel algorithms for short-range molecular dynamics. *J. Comp. Phys.* 117, 1–19, see also <http://lammps.sandia.gov/index.html>.
- Ribberink, J. S., 1998. Bed-load transport for steady flows and unsteady oscillatory flows. *Coastal Engineering* 34 (1), 59–82.
- Saffman, P., 1965. The lift on a small sphere in a slow shear flow. *Journal of Fluid Mechanics* 22 (02), 385–400.
- Schmeeckle, M. W., 2014. Numerical simulation of turbulence and sediment transport of medium sand. *Journal of Geophysical Research: Earth Surface* 119, 1240–1262.
- Scholtès, L., Chareyre, B., Michallet, H., Catalano, E., Marzougui, D., 2015. Modeling wave-induced pore pressure and effective stress in a granular seabed. *Continuum Mechanics and Thermodynamics* 27 (1-2), 305–323.

- Sun, J., Battaglia, F., Subramaniam, S., 2007. Hybrid two-fluid DEM simulation of gas-solid fluidized beds. *Journal of Fluids Engineering* 129 (11), 1394–1403.
- Sun, J., Sundaresan, S., 2011. A constitutive model with microstructure evolution for flow of rate-independent granular materials. *Journal of Fluid Mechanics* 682, 590.
- Sun, R., Xiao, H., 2015a. Diffusion-based coarse graining in hybrid continuumdiscrete solvers: Applications in CFD–DEM. *International Journal of Multiphase Flow* 72, 233–247.
- Sun, R., Xiao, H., 2015b. Diffusion-based coarse graining in hybrid continuumdiscrete solvers: Theoretical formulation and a priori tests. *International Journal of Multiphase Flow* 77, 142 – 157.
- Sun, R., Xiao, H., 2016a. CFD–DEM simulations of current-induced dune formation and morphological evolution. *Advances in Water Resources* 92, 228 – 239.
- Sun, R., Xiao, H., 2016b. Sedifoam: A general-purpose, open-source CFD–DEM solver for particle-laden flow with emphasis on sediment transport. *Computers & Geosciences* 89, 207 – 219.
- Syamlal, M., Rogers, W., O’Brien, T., 1993. MFIx documentation: Theory guide. Tech. rep., National Energy Technology Laboratory, Department of Energy, see also URL <http://www.mfix.org>.
- Tsuji, Y., Kawaguchi, T., Tanaka, T., 1993. Discrete particle simulation of two-dimensional fluidized bed. *Powder Technology* 77 (79-87).
- van Rijn, L., 1984. Sediment transport, part I: Bed load transport. *Journal of hydraulic engineering* 110 (10), 1431–1456.
- Yang, R., Zou, R., Yu, A., 2002. Voronoi tessellation of the packing of fine uniform spheres. *Physical Review E* 65 (4), 041302.
- Yang, R. Y., Zou, R. P., Yu, A. B., 2003. Microdynamic analysis of particle flow in a horizontal rotating drum. *Powder Technology* 130 (1), 138–146.

- Yi, L. Y., Dong, K. J., Zou, R. P., Yu, A. B., 2011. Coordination number of the packing of ternary mixtures of spheres: DEM simulations versus measurements. *Industrial & Engineering Chemistry Research* 50 (14), 8773–8785.
- Yoshizawa, A., Horiuti, K., 1985. A statistically-derived subgrid-scale kinetic energy model for the large-eddy simulation of turbulent flows. *Journal of the Physical Society of Japan* 54 (8), 2834–2839.
- Zhao, J., Shan, T., 2013. Coupled CFD–DEM simulation of fluid–particle interaction in geomechanics. *Powder Technology* 239, 248–258.

Appendix. A

The definitions and the post-processing procedures of the micromechanic variables, including Voronoi solid volume fraction and coordination number, are detailed in this appendix.

A.1 Voronoi Volume Fraction

The Voronoi cell is defined according to the Voronoi diagram in Figure A.1. The Voronoi cell of a spherical sediment particle is the region that is closer to the center of this spherical particle than other points in the system (Yang et al., 2002). It can be seen in the figure that the regions highlighted with filled color are the Voronoi cells, numbering from 1 to 5. The 3D Voronoi cells are created by taking pairs of points that are close together and drawing a plane that is equidistant between them and perpendicular to the line connecting them. This region is considered a free volume for the particle to move. The Voronoi solid volume fraction is the ratio between the volume of the particle and the Voronoi cell. The calculation of the Voronoi solid volume fraction is based on the Voronoi package of LAMMPS (Plimpton, 1995).

A.2 Coordination Number

The coordination number of a sediment particle is defined as the number of nearest neighbors of the particle. Figure A.2 shows the coordination number of different packing configurations. The coordination number is useful in the investigation of the momentum and heat transfer of

the particles. This quantity is also useful in particulate flow in the evaluation of the structural properties of packing particles, such as tensile strength, thermal conductivity, solid-solid reactions, phase formation, and permeability (Yi et al., 2011).

A.3 Spatial Averaging Procedure

The vertical profiles of the Voronoi volume fraction and coordination number are obtained by averaging the information of individual particles. According to Gupta (2015), the quantities are averaged by using:

$$\zeta(\mathbf{x}) = \sum_{i=1}^{N_p} \mathcal{Z}_i h_i(\mathbf{x}_i), \quad (\text{A.1})$$

where ζ is the quantity obtained after the averaging procedure; \mathcal{Z}_i is the same quantity of the sediment particle before the averaging; N_p is the number of particles in the cell; \mathbf{x} is the location of the cell; \mathbf{x}_i is the location of particle i . The function $h_i(\mathbf{x}_i)$ is defined as:

$$h_i(\mathbf{x}_i) = \frac{1}{(b^2\pi)^{3/2}} \exp \left[-\frac{(\mathbf{x} - \mathbf{x}_i)^T(\mathbf{x} - \mathbf{x}_i)}{b^2} \right], \quad (\text{A.2})$$

where $b = 4d_p$ is the bandwidth of the averaging. In this paper, the resolution of the post-processing grid is $1 \times 30 \times 1$ (in streamwise, vertical, and lateral directions, respectively). The size of the cell in the vertical direction is the particle diameter d_p . Therefore, the maximum height of the post-processing grid is $30d_p$, which is higher than the maximum height reached by the sediment particles. Since the resolution of post-processing mesh in streamwise and lateral direction is 1, the results are horizontally-averaged.

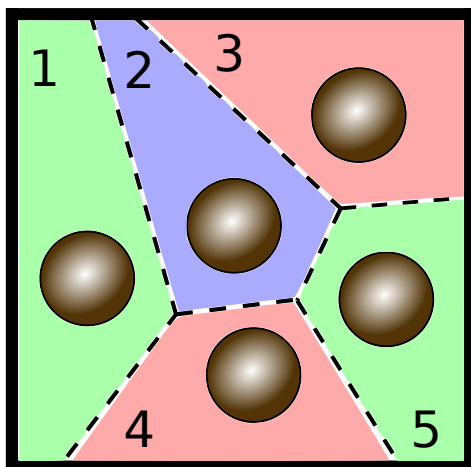


Figure A.1: 2D Voronoi cell of sediment particles.

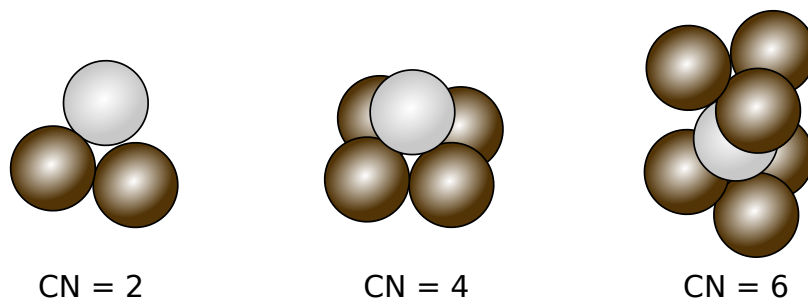


Figure A.2: The coordination number (CN) of the light particle in different packing regimes.